

CrossMark
click for updatesCite this: *J. Mater. Chem. A*, 2015, 3,
9171

Temperature dependence of hole conductor free formamidinium lead iodide perovskite based solar cells†

Sigalit Aharon, Alexander Dymshits, Amit Rotem and Lioz Etgar*

Organometal halide perovskite is a promising material in photovoltaic (PV) cells. Within a short time, its performance has increased dramatically to become a real competitor to silicon solar cells. Here we report on the temperature dependence (annealing temperature and the dependence of the photovoltaic parameters on temperature) of formamidinium (FA) lead iodide (FAPbI₃), methylammonium (MA) lead iodide (MAPbI₃) and their mixture (MAPbI₃ : FAPbI₃) in hole conductor free perovskite solar cells. These three types of perovskites function both as light harvesters and as hole conductors. Surface photovoltage and optical characterization reveal the p-type behavior and the band gap of the different perovskites. We observed that the ratio between the MA and FA cations might change during the annealing process, affecting the band gap and the stability of the layers. The PV parameters at different temperatures show better stability for the pure MAPbI₃ and FAPbI₃ solar cells compared to their mixture. Using intensity modulated photovoltage/photocurrent spectroscopy, we found that the diffusion length is weakly dependent on the light intensity, while the charge collection efficiency drops with light intensity for the FAPbI₃-based cells. However, for MAPbI₃ and the mixture, the charge collection efficiency remains constant for a wide range of light intensities.

Received 28th September 2014
Accepted 14th October 2014

DOI: 10.1039/c4ta05149a

www.rsc.org/MaterialsA

Introduction

Finding solutions for alternative energy is perhaps the biggest challenge of our century, and this encompasses the search for promising photovoltaic (PV) technology. Simple, inexpensive production methods are the key to developing and producing PV cells as a widespread technology. Recently, a breakthrough occurred in the photovoltaic field by using organometal halide perovskite as a light harvester in the solar cell.¹ Organometal halide perovskite has a large absorption coefficient in the visible region,² high carrier mobility,^{3,4} and a tunable band gap energy (E_g), facilitating its use as a light harvester in a solar cell.⁵ In addition, organometal halide perovskite can be prepared using simple, low-temperature solution processes.⁶

In recent years, intensive work has been carried out on the perovskite structure, the solar cell structure, and on the deposition techniques of different active layers,^{7–16} currently achieving an efficiency of approximately 17.9%.¹⁷ Moreover, due to its distinctive properties, perovskite solar cells without a hole conductor were demonstrated to achieve a power conversion efficiency (PCE) of 10.8%.^{18–21} Characterizations of the perovskite-based solar cells have led to a better understanding of cell

architectures, and the mechanisms of electrical processes and phenomena within the cell.^{22–26}

The general perovskite structure is of the form ABX₃. In the case of hybrid organic–inorganic lead halide perovskites, A is an organic cation, B is lead (Pb) and X is a negatively charged halide. As stated by Shockley and Queisser, the E_g of the absorber strongly affects the performance of the cell.²⁷ It has been demonstrated that the size of the organic cation influences the E_g of the resulting perovskite by affecting the B–X–B angle.²⁸ Furthermore, Snaith *et al.* showed that the E_g of the perovskite changes by altering the B–X bond length. Alterations in the B–X bond length can be caused by changing the halide, the metal, or the cation size.²⁹ In particular, by changing the cation from methylammonium (CH₃NH₃⁺, MA⁺) to a larger formamidinium (NH₂CH=NH₂⁺, FA⁺) cation, the band gap of the perovskite decreases; this was also supported by the higher Goldschmidt tolerance factor in the case of the FA⁺ cation.³⁰ In a recent study, perovskite compositions of (MA)_x(FA)_{1–x}PbI₃ (0 < x < 1) were used to extend the optical absorption onset into the red region, for the enhancement of solar light harvesting.³¹ It was found that the single-cation perovskite phase has shorter carrier diffusion lengths than the double-cation perovskite. The band gap tunability between 1.48 and 2.23 eV was demonstrated by changing the MA⁺ cation with FA⁺ and Cs. A PCE of 14.2% was achieved using FAPbI₃ as the absorber in the cell with Spiro-OMeTAD as the hole conductor.²⁸ In addition, the

The Hebrew University of Jerusalem, Institute of Chemistry, Casali Center for Applied Chemistry, Jerusalem 91904, Israel. E-mail: lioz.etgar@mail.huji.ac.il

† Electronic supplementary information (ESI) available. See DOI: 10.1039/c4ta05149a

crystallization of $\text{FAPbI}_{(3-x)}\text{Cl}_x$ ($1 < x < 3$) was studied using the two-step deposition at various annealing temperatures.^{29,32}

In this work, we report for the first time about hole-conductor-free (MA/FA)PbI₃-based solar cells, where the (MA/FA)PbI₃ acts both as a light harvester and as a hole transporter. The two-step deposition was used to fabricate MAPbI₃, FAPbI₃ and MAPbI₃ : FAPbI₃ = 1 : 1 perovskites as the light harvester in the solar cell. The effect of composition and annealing temperature on the photovoltaic performance (PV) was studied. Surface photovoltage spectroscopy was used to elucidate the electronic behavior of these perovskites. Intensity modulated photovoltage spectroscopy (IMVS) and intensity modulated photocurrent spectroscopy (IMPS) were used to reveal more details about the diffusion length, charge collection efficiency and recombination lifetime. Moreover, the PV performance of the cells was measured at various temperatures. Analyzing the solar cell performance at different temperatures in the range of 22 °C–95 °C is highly important: first, the organic part of the hybrid perovskite is mobile in this range of temperatures³³ which could affect the PV performance. Second, in practice the solar cell should be working in this range of temperatures (*e.g.* on roofs, inside cars, *etc.*). Therefore, analyzing the PV performance at different temperatures should provide essential information on the cell behavior under working conditions.

Experimental section

Methods and device fabrication

Precursor synthesis. Methyl ammonium iodide (MAI) was synthesized by reacting 27.8 mL of methylamine (40% in methanol, TCI) with 30 mL of hydriodic acid (57 wt% in water, Aldrich) in a 250 mL round bottom flask at 0 °C for 2 h under stirring. The precipitate was recovered by placing the solution on a rotary evaporator and carefully removing the solvents at 50 °C for 1 h. The white raw product of MAI was washed with ethanol by stirring the mixture for 30 minutes. Then the mixture was filtered and washed with diethylether. The washing step was repeated three times. After filtration, the solid was collected and dried at 60 °C in a vacuum oven for 24 h. Formamidinium iodide (FAI) was synthesized by reacting 0.33 g mL⁻¹ solution of formamidinium acetate (FAAc, 99%, Aldrich) in methanol absolute (Aldrich) with 6.5 mL of HI. The reaction conditions were similar to those of MAI preparation, apart from the reaction duration, which was 5 h. The cleaning procedure was similar to that of MAI.

Device fabrication. The substrate of the device was a $\text{SnO}_2\text{:F(FTO)}$ conducting glass (15 Ω cm⁻¹, Pilkington). A blocking layer was deposited on the FTO glass using a solution of titanium diisopropoxidebis(acetylacetonate) (TiDIP, 75% in isopropanol, Aldrich) in ethanol. The TiDIP solution was spin coated and then annealed at 450 °C for 30 min. The TiO₂ nanoparticle solution was spin coated and annealed at 500 °C for 30 min subsequent to TiCl₄ treatment for 30 min at 70 °C and annealing at 500 °C for 30 min. For the perovskite layer, PbI₂ was dissolved in DMF, dropped onto the TiO₂ film and spin coated followed by annealing at 90 °C for 30 min. In the second step, the cell was dipped into the dipping solution of 10.0 mg mL⁻¹

MAI in isopropanol, or 10.7 mg mL⁻¹ FAI in isopropanol, or 5.0 mg MAI + 5.3 mg FAI per mL isopropanol (molar ratio of FAI : MAI = 1 : 1). Following the dipping step, the samples were annealed at two different temperatures, according to the dip solution that was used for their preparation. For samples that were dipped in MAI solution, the annealing temperature was 100 °C (for 30 minutes), while for the samples that were dipped in FAI solution or in FAI : MAI = 1 : 1 solution, the annealing temperature was 175 °C (for 15 minutes). During dipping and annealing, MAPbI₃ and FAPbI₃ were formed, indicated by the dark brown color of the electrodes. Finally, the back contact was deposited by evaporating 40 nm of gold under a pressure of 5 × 10⁻⁶ Torr. The active area was 0.09 cm².

X-ray diffraction. X-ray powder diffraction measurements were performed in grazing incidence X-ray diffraction (GIXRD) mode on a D8 Advance Diffractometer (Bruker AXS, Karlsruhe, Germany) with a goniometer radius of 217.5 mm, a secondary graphite monochromator, 2° Soller slits and a 0.2 mm receiving slit. XRD patterns within the range 5° to 60° 2 θ were recorded at room temperature using CuK α radiation (1 1/4 1.5418 Å) with the following measurement conditions: a tube voltage of 40 kV, tube current of 40 mA, step-scan mode with a step size of 0.02° 2 θ and counting time of 1–3 s per step. The value of the grazing incidence angle was 2.5°.

Photovoltaic characterization. Photovoltaic measurements were performed on a New Port system, composed of an Oriel *I-V* test station using an Oriel Sol3A simulator. The solar simulator was class AAA for spectral performance, uniformity of irradiance, and temporal stability. The solar simulator was equipped with a 450 W xenon lamp. The output power was adjusted to match AM1.5 global sunlight (100 mW cm⁻²). The spectral match classifications were IEC60904-9 2007, JIC C 8912, and ASTM E927-05. *I-V* curves were obtained by applying an external bias to the cell and measuring the generated photocurrent with a Keithley model 2400 digital source meter. The voltage step and delay time of the photocurrent were 10 mV and 40 ms, respectively. Oriel IQE-200 was used to determine the monochromatic incident photon-to-electric current conversion efficiency. Under full computer control, light from a 150 W xenon arc lamp was focused through a monochromator in the 300–1800 nm wavelength range onto the photovoltaic cell under test. The monochromator was incremented through the visible spectrum to generate the IPCE (*l*) as defined by $\text{IPCE} (l) = 12\,400 (J_{sc}/l\Phi)$, where *l* is the wavelength, *J*_{sc} is the short-circuit photocurrent density (mA cm⁻²), and Φ is the incident radiative flux (mW cm⁻²). Photovoltaic performance was measured by using a metal mask with an aperture area of 0.09 cm².

Absorption measurements. The UV-vis absorption spectra were recorded using a Jasco V-670 spectrophotometer.

Ultra high resolution scanning electron microscopy (UHR-SEM). The images were obtained using a Sirion UHR SEM from FEI (Field Emission Instruments, The Netherlands). The measurement conditions were 5 kV at various magnifications, as seen on the data bar of the images.

Surface photovoltage spectroscopy (SPS). SPS measurements were performed using the SKP5050-SPS040 system. The contact potential difference (CPD), between the sample and the

vibrating tip (gold tip), was measured by the Kelvin probe method. Samples were measured inside a dark Faraday cage. For SPS measurements, the samples were illuminated by a 150 W quartz tungsten halogen lamp. The wavelength resolution was 2 nm. Before measurement, samples were stabilized with a tip for about an hour. The scan direction was from long to short wavelength. All values were calculated with an average of 30 single measurements that were repeated three times ($30 \times 3 = 90$).

Nuclear magnetic resonance (NMR). NMR spectra were acquired using a spectrometer Bruker DRX 400.

Intensity modulated photovoltage spectroscopy (IMVS) and intensity modulated photocurrent spectroscopy (IMPS). The photocarrier recombination (transfer) times at open circuit (short circuit) were measured by IMVS (IMPS). The IMVS (IMPS) measurements were performed using an Autolab FRA32M LED driver equipped with a red light source (627 nm), illuminating from the substrate side. The photovoltaic cells were illuminated with a bias light intensity with a sinusoidal wave modulation. The amplitude of the modulated photo voltage (photocurrent) density was kept at 10% or lower compared to the steady-state photovoltage (photocurrent) density, with frequencies ranging from 1 Hz to 20 kHz.

Results and discussion

This work describes two different perovskite cations, FA and MA, in a hole-conductor-free perovskite based solar cell. NMR and X-ray diffraction (XRD) confirm the structure of the cations (Fig. 1D and S1†). The two different perovskites functioned both as light harvesters and as hole conductors. The structure of the

hole-conductor-free perovskite solar cell is composed of FTO glass/TiO₂ compact layer/mesoporous TiO₂/perovskite/gold, as presented in Fig. 1A. Perovskites were deposited by two-step deposition where MAPbI₃, FAPbI₃, and a mixture of (MA : FA) PbI₃ with a ratio of 1 : 1 were studied. During illumination, the electrons are injected into the mesoporous TiO₂ from the light harvester material (*i.e.* the perovskites, which could be MAPbI₃, FAPbI₃, or their mixture), and the holes are transported to the gold contact.¹⁷ Electron injection and hole transport is possible for the three perovskite compositions. The experiments in this work are based on 15 cells for each characterization technique and for each type of perovskite.

It was previously reported that changing the cation from FA to MA could tune the band gap of the material.²⁹ To determine the band gap, optical measurements and Surface Photovoltage Spectroscopy (SPS) were used.^{34,35} The SPV/SPS experiment is based on the classical Kelvin probe technique, which measures the difference in work functions (also known as the contact potential difference (CPD)) between a metallic reference probe and the semiconductor surface. The distance between the reference electrode and semiconductor is a few millimeters while a capacitor arrangement is formed. Once the metallic probe vibrates, an AC capacitance is formed between the probe and the semiconductor resulting in an AC current in the external circuit. This AC current is zero if and only if there is no charge on the capacitor. In this case, the CPD must be zero. When a DC bias is applied it nullifies the AC current. Thus, the applied DC bias is equal and opposite to the CPD.

In this work, the scanned surfaces were MAPbI₃, FAPbI₃, and a mixture of both which had a 1 : 1 molar ratio. Fig. 2C shows the Δ CPD vs. the energy in eV of the studied samples. The first observation that arises from the SPS spectra in Fig. 1C is that MAPbI₃ and FAPbI₃ (and their mixture) are p-type semiconductors. This is because of the fact that in the case of p-type semiconductors there is a downward band-bending of the conduction band towards the surface at the junction between the metal and the semiconductor (whereas in the case of n-type semiconductors, an upward band-bending occurs). Once the applied energy is higher than the band gap, the bending is decreased, meaning that there is a positive Δ CPD in p-type semiconductors (and negative Δ CPD in the case of n-type semiconductors).³⁶ This can be seen by the sign of the knee associated with the surface photovoltage onset.

In addition to the electronic behavior of the different perovskites, the band gap energy of each material can be extracted using the SPS spectra. The SPS method is immune to reflection or scattering losses; only photons that are absorbed in the sample contribute to the SPS signal. In this case, the signal onset starts at photon energies close to the band gap of the perovskite samples (FAPbI₃, MAPbI₃ and their mixture). As a result, it can be concluded that the perovskite samples have fewer sub-band gap states (relative to TiO₂, see ref. 33). The band gaps (E_g) of MAPbI₃, FAPbI₃ and their mixture are estimated to be 1.57 eV, 1.45 eV and 1.53 eV, respectively (error of ± 0.01 eV). It is important to note that the SPS measurements were performed under high level of accuracy, as detailed in the Experimental section.

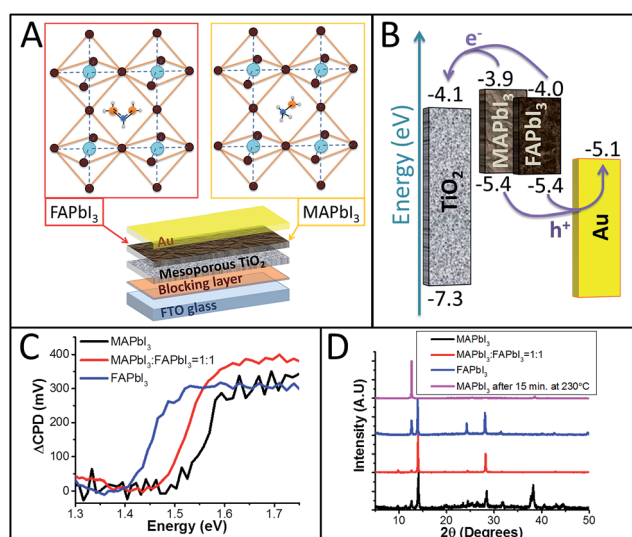


Fig. 1 (A) The structure of the cell: FTO glass/blocking layer (compact TiO₂)/mesoporous TiO₂/hybrid organic-inorganic perovskite/gold. The layer of perovskite contains MAPbI₃, FAPbI₃, or a mixture of both. The colors in the crystalline structures represent Pb (light blue), iodide (brown), carbon (blue), nitrogen (orange) and hydrogen (white). (B) Energy levels of the different layers of the cell.^{31,37} (C) SPS measurement of the different perovskites. (D) XRD of the different samples: MAPbI₃, MAPbI₃ : FAPbI₃ = 1 : 1, FAPbI₃, and MAPbI₃ after 15 min at 230 °C.

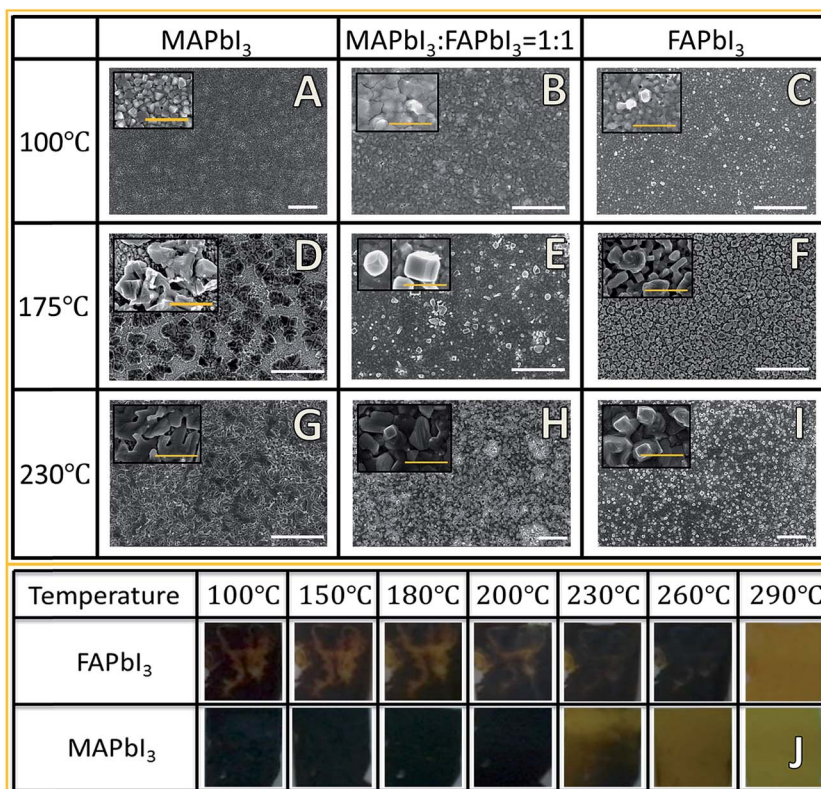


Fig. 2 UHR-SEM images of the perovskite compositions at various annealing temperatures (100 °C, 175 °C and 230 °C). The white scale bar is 5 μm and the orange scale bar (inset) is 1 μm . (A) MAPbI₃ annealed at 100 °C. (B) MAPbI₃ : FAPbI₃ = 1 : 1 annealed at 100 °C. (C) FAPbI₃ annealed at 100 °C. (D) MAPbI₃ annealed at 175 °C. (E) MAPbI₃ : FAPbI₃ = 1 : 1 annealed at 175 °C. (F) FAPbI₃ annealed at 175 °C. (G) MAPbI₃ annealed at 230 °C. (H) MAPbI₃ : FAPbI₃ = 1 : 1 annealed at 230 °C. (I) FAPbI₃ annealed at 230 °C. (J) Pictures of the samples of MAPbI₃ or FAPbI₃ on glass after annealing at various temperatures.

The band gaps of the perovskites were also estimated using Tauc plots by manipulating transparency measurements of the perovskite films (The Tauc plots are represented in Fig. S2 in the ESI†). The E_g values of MAPbI₃, FAPbI₃ and their mixture obtained by the Tauc plot analysis are 1.56 eV, 1.46 eV and 1.54 eV, respectively (error of ± 0.01 eV, resulted by the linear fitting). There is good agreement between the results of the two methods, and this fact supports the validity of each one of the methods.

Moreover, the results are in good agreement with theory, which predicts that the larger the cation, the smaller the E_g .²⁹ The XRD spectra of the three perovskites are presented in Fig. 1D. The fact that the mixture shows peaks from both samples (MAPbI₃ and FAPbI₃) indicates that a mixture of the two samples was formed. In addition the E_g of the mixture is between the band gap energies of MAPbI₃ and FAPbI₃ which further support this claim.

Fig. 2 shows XHR-SEM images of the perovskites at various annealing temperatures. Fig. 2A, D and G show MAPbI₃ at various annealing temperatures. According to the images, the best coverage was achieved at 100 °C which supports the previous report.³² While at 175 °C the coverage was not as good as at 100 °C. At 230 °C, MAPbI₃ decomposes to PbI₂ as can be seen by the XRD analysis shown in Fig. 1D (purple line), which was performed for the sample after annealing for 15 minutes at

230 °C.²⁰ The mixture (Fig. 2B, E and H) shows good coverage for all annealing temperatures. The presence of the two perovskite crystals, MAPbI₃ and FAPbI₃, is observed in the inset of Fig. 2E, corresponding to an annealing temperature of 175 °C which further support the XRD spectra of the mixture as shown in Fig. 1D. For FAPbI₃ (Fig. 2C, F and I), the crystals are hardly recognizable at 100 °C while at 175 °C and 230 °C the FAPbI₃ crystals are observed clearly, supporting the required high annealing temperature of the FAPbI₃ perovskite.

Further investigation of the dependence of FAPbI₃ and MAPbI₃ films at various temperatures can be seen in Fig. 2J. Seven different temperatures (100 °C, 150 °C, 180 °C, 200 °C, 230 °C, 260 °C and 290 °C) were tested. Early reports showed that in the two-step deposition method, an annealing temperature of ~ 170 °C (ref. 32) is used for the FAPbI₃ perovskite, while for MAPbI₃, the annealing temperature is 70 °C–100 °C.²⁹

As indicated in Fig. 2J, the MAPbI₃ perovskite has a dark color until 200 °C, while at ~ 230 °C, the MAPbI₃ started to decompose. On the other hand, the FAPbI₃ perovskite has a dark color till 260 °C, while at 290 °C, it decomposes. According to these results, an annealing temperature of ~ 175 °C is suitable for a mixture of FAPbI₃ with MAPbI₃. This observation is in good agreement with the XHR-SEM images. Consequently, it is reasonable that the side reactions (such as sublimation, evaporation and decomposition of MAPbI₃ and FAPbI₃) could take

place in the mixture samples. The direct observation of these reactions is that despite the fact that the original molar ratio of MAPbI_3 : FAPbI_3 in the dipping solution was 1 : 1, it can be that the actual molar ratio between MAPbI_3 and FAPbI_3 after the annealing process is not 1 : 1. According to the stability test we performed, it is reasonable to estimate that the portion of FAPbI_3 is a bit larger than that of MAPbI_3 . MAPbI_3 , which has the smaller cation, is more likely to be affected by the high temperature. In other words, the side reaction could be expected to diminish the MAPbI_3 content more dramatically than the FAPbI_3 content.

Fig. 3A and B present the current–voltage curves and the external quantum efficiency (EQE) spectra of the hole conductor free cells, respectively. The highest current density was observed for the MAPbI_3 -based cells while the lowest current density was observed for the FAPbI_3 -based cells. A reason for the difference in the current density might be due to the difference between the MAPbI_3 conduction band (CBM) and the TiO_2 CBM which is bigger than the difference between the FAPbI_3 CBM and the TiO_2 CBM. On the other hand, the open circuit voltage (V_{oc}) of the cells is similar. The EQE spectra show a longer wavelength response when perovskites contain the FA cation.

Fig. 4A and 4B present the photovoltaic parameters of the complete hole-conductor-free MAPbI_3 , FAPbI_3 and the mixture (MAPbI_3 : FAPbI_3) solar cells measured at eight different temperatures: (22 °C, 35 °C, 45 °C, 55 °C, 65 °C, 75 °C, 85 °C, and 95 °C).

The general trend that is reflected from this analysis is similar for all the cells. The J_{sc} of all samples increased as temperature increases. Increasing the temperature of a semiconductor results in a decrease of the E_g which could influence the J_{sc} . It can be seen that the J_{sc} increases by more than 30% in the case of FAPbI_3 . This is expected due to the better stability of FAI at high temperatures. The MAPbI_3 has an initial increase of 20% in J_{sc} while the FAPbI_3 stays stable for the rest of the temperature range. An interesting point is that the cells which used a mixture of MAPbI_3 and FAPbI_3 showed the most severe degradation of the PV parameters with the increase in temperature. A possible explanation for this phenomenon is that the increase in temperature harmed the crystals from the inside. The active layer included a combination of MA^+ and FA^+ in the crystal voids. The two cations are affected differently by the temperature increase, and this

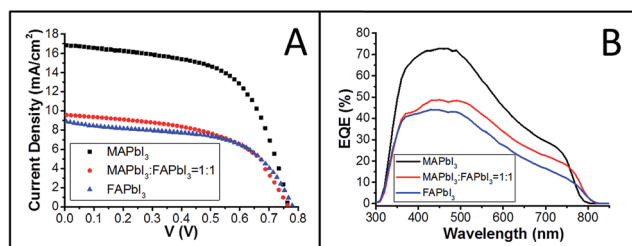


Fig. 3 (A) The current–voltage curves of the different perovskite solar cells under 1 sun illumination. (B) External Quantum Efficiency (EQE) for the different perovskite solar cells.

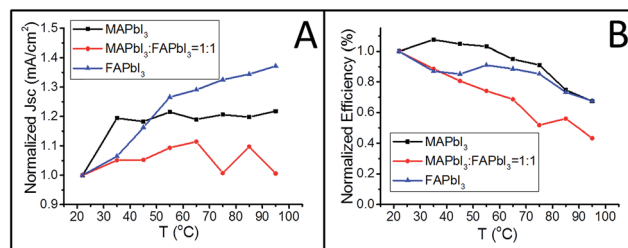


Fig. 4 (A) The normalized short circuit current density (J_{sc}) of the three different photovoltaic cells at various temperatures. (B) The normalized efficiency of the photovoltaic cells at various temperatures.

difference could lead to the formation of strain inside the crystalline structure. Such a strain could be harmful when measuring the photovoltaic performance of the cell at varying temperatures. In contrast to the temperature dependence on J_{sc} , the efficiency decreased as the temperature increased (Fig. 4B). This behavior is due to the decrease in the FF and the V_{oc} . When increasing the temperature, the recombination increases, resulting in a decrease of the V_{oc} . Additional contribution to the decrease of the V_{oc} can be related to the increase of the intrinsic carrier when the temperature increases. The intrinsic carrier concentration depends on the band gap, lowering the band gap giving higher intrinsic concentration which can result in lower V_{oc} .

Also in this case, the mixture showed the lowest results regarding temperature dependence. The increase in J_{sc} does not compensate for the decrease in the FF and the V_{oc} , and as a result, the efficiency decreases.^{38,39}

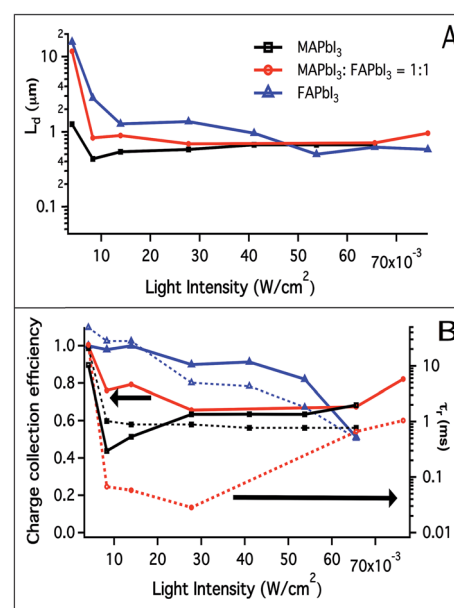


Fig. 5 (A) Diffusion length (L_d) as a function of light intensity for the cells studied. (B) Charge collection efficiency and recombination lifetime (τ_r) as a function of light intensity. The dashed lines correspond to the recombination lifetime.

Table 1 Photovoltaic parameters of the cells with the perovskites, and the band gap energy that was extracted from SPS and the Tauc plot

Active layer	V_{oc} (V)	J_{sc} (mA cm ⁻²)	FF (%)	Efficiency (%)	$E_{g,SPS}$ (eV)	$E_{g,Tauc\ plot}$ (eV)
MAPbI ₃	0.77	16.84	60	7.7	1.57	1.56
MAPbI ₃ : FAPbI ₃ = 1 : 1	0.77	9.58	54	4.0	1.53	1.54
FAPbI ₃	0.78	8.96	56	3.9	1.45	1.46

Intensity modulated photocurrent/photovoltage spectroscopies were used to measure the transport and recombination times (t and τ , respectively) of the solar cells studied. The electron diffusion length L_d in the perovskite solar cell can be determined using the expression^{40–42} $L_d = (\tau_r D)^{1/2}$ where D is the diffusion coefficient and τ_r is the recombination lifetime. The electron diffusion length represents the average distance which the electron travels before it recombines with holes in the perovskite or at the back contact. Fig. 5A shows the diffusion length calculated using IMVS and IMPS as a function of the light intensity. At low light intensity, all cells have a higher diffusion length, although the FAPbI₃ and the mixture have a longer initial diffusion length. When increasing the light intensity, all cells decreased to the same diffusion length of around 0.8–1 μm (this result is in good agreement with the literature). There is a weak light intensity dependence of the diffusion length. The diffusion length varies by less than a factor of 1 over more than seven decades of light intensity, similar to the dependence of the diffusion length by the light intensity in dye sensitized solar cells.⁴³

The charge collection efficiency and the recombination lifetime are presented in Fig. 5B. The charge collection efficiency can be calculated using⁴⁴ $\eta_{cc} = 1 - \tau_t/\tau_r$. The FAPbI₃ cell starts with a high η_{cc} at low light intensity and drops to 0.5 at higher intensities. On the other hand, the MAPbI₃ and the mixture have low η_{cc} at low intensities, which increases to 0.7–0.8 at higher light intensities. These results explain well the PV performance of these cells at 1 sun illumination (see Table 1). Moreover the recombination lifetime (presented as dashed lines in Fig. 5B) decreases when increasing the light intensity as expected. However, for the MAPbI₃ cell, the recombination lifetime remains constant for most of the intensity ranges which supports the high efficiency observed for the MAPbI₃-based cells.

Conclusions

FAPbI₃, MAPbI₃ and their mixture were studied in hole-conductor-free solar cells, where all the perovskites studied function as light harvesters and hole conductors. SPS measurements determined the electronic behavior and the energy gaps of the perovskites. Temperature dependence measurements show that the initial ratio between the MA and the FA cations is not necessarily defined as the final material composition. The change in the J_{sc} and the efficiency at various temperatures show superior stability for the FAPbI₃ based cells. A diffusion length of 0.8–1 μm was observed for all perovskites at a wide range of light intensities measured by IMVS and IMPS

techniques. This work provides useful information for the design and understanding of stable, high efficiency perovskite-based solar cells.

Acknowledgements

We would like to thank the Israel Alternative Energy Foundation (I-SAEF) that financed this research, the Ministry of Industry Trade and Labor Office of the Chief Scientist Kamin project no.50303, and the Tashtiot project of the Office of the Chief Scientist.

References

- 1 A. Kojima, K. Teshima, Y. Shirai and T. Miyasaka, Organometal Halide Perovskites as Visible-Light Sensitizers for Photovoltaic Cells, *J. Am. Chem. Soc.*, 2009, **131**, 6050–6051.
- 2 A. Kojima, M. Ikegami, K. Teshima and T. Miyasaka, Highly Luminescent Lead Bromide Perovskite Nanoparticles Synthesized with Porous Alumina Media, *Chem. Lett.*, 2012, **41**, 397–399.
- 3 C. R. Kagan, D. B. Mitzi and C. D. Dimitrakopoulos, Organic-Inorganic Hybrid Materials as Semiconducting Channels in Thin-Film Field-Effect Transistors, *Science*, 1999, **286**, 945–947.
- 4 D. B. Mitzi, C. A. Feild, Z. Schlesinger and R. B. Laibowitz, Transport Optical and Magnetic properties of the Conducting Halide Perovskite CH₃NH₃SnI₃, *J. Solid State Chem.*, 1995, **114**, 159–163.
- 5 E. Mosconi, A. Amat, M. K. Nazeeruddin, M. Grätzel and F. D. Angelis, First-Principles Modeling Of Mixed Halide Organometal Perovskites For Photovoltaic Applications, *J. Phys. Chem. C*, 2013, **117**, 13902–13913.
- 6 K. Liang, D. B. Mitzi and M. T. Prikas, Synthesis and Characterization of Organic-Inorganic Perovskite Thin Films Prepared Using a Versatile Two-Step Dipping Technique, *Chem. Mater.*, 1998, **10**, 403–411.
- 7 Z. Xiao, C. Bi, Y. Shao, Q. Dong, Q. Wang, Y. Yuan, C. Wang, Y. Gao and J. Huang, Efficient High Yield Perovskite Photovoltaic Devices Grown by Interdiffusion of Solution-Processed Precursore Stacking Layers, *Energy Environ. Sci.*, 2014, **7**, 2619–2623.
- 8 A. Abate, M. Saliba, D. J. Hollman, S. D. Stranks, K. Wojciechowski, R. Avolio, G. Grancini, A. Petrozza and H. J. Snaith, Supramolecular Halogen Bond Passivation of Organic-Inorganic Halide Perovskite Solar Cells, *Nano Lett.*, 2014, **14**(6), 3247–3254, DOI: 10.1021/nl500627x.

- 9 D. Bi, S. J. Moon, L. Haggman, G. Boschloo, L. Yang, E. M. J. Johansson, M. K. Nazeerudin and M. Graetzel, Using a Two-Step Deposition Technique to Prepare Perovskite ($\text{CH}_3\text{NH}_3\text{PbI}_3$) for Thin Film Solar Cells Based on ZrO_2 and TiO_2 Mesostuctures, *RSC Adv.*, 2013, **3**, 18762–18766.
- 10 G. E. Epron, V. M. Burlakov, A. Goriely and H. J. Snaith, Neutral Color Semitransparent Microstructured Perovskite Solar Cells, *ACS Nano*, 2014, **8**(1), 591–598, DOI: 10.1021/nn4052309.
- 11 G. E. Epron, V. M. Burlakov, P. Docampo, A. Goriely and H. J. Snaith, Morphological Control for High Performance, Solution-Processed Planar Heterojunction Perovskite Solar Cells, *Adv. Funct. Mater.*, 2014, **24**, 151–157, DOI: 10.1002/adfm.201302090.
- 12 J. H. Noh, S. H. Im, J. H. Heo, T. N. Mandal and S. I. Seok, Chemical Management for Colorful, Efficient, and Stable Inorganic–Organic Hybrid Nanostructured Solar Cells, *Nano Lett.*, 2013, **13**, 1764–1769.
- 13 J. H. Im, C. R. Lee, J. W. Lee, S. W. Park and N. G. Park, 6.5% Efficient Perovskite Quantum-Dot-Sensitized Solar Cell, *Nanoscale*, 2011, **3**, 4088–4093.
- 14 L. Etgar, P. Gao, Z. Xue, Q. Peng, A. K. Chandiran, B. Liu, M. K. Nazeeruddin and M. Graetzel, Mesoscopic $\text{CH}_3\text{NH}_3\text{PbI}_3/\text{TiO}_2$ Heterojunction Solar Cells, *J. Am. Chem. Soc.*, 2012, **134**, 17396–17399.
- 15 J. Qiu, Y. Qiu, K. Yan, M. Zhong, C. Mu, H. Yan and S. Yang, All-Solid-State Hybrid Solar Cells Based on a New Organometal Halide Perovskite Sensitizer and One-Dimensional TiO_2 Nanowire Arrays, *Nanoscale*, 2013, **5**, 3245–3248.
- 16 C. Zuo and L. Ding, An 80.11% FF record achieved for perovskite solar cells by using the NH_4Cl additive, *Nanoscale*, 2014, **6**, 9935.
- 17 http://www.nrel.gov/ncpv/images/efficiency_chart.jpg.
- 18 W. Abu-Laban and L. Etgar, Depleted Hole Conductor-Free Lead Halide Iodide Heterojunction Solar Cells, *Energy Environ. Sci.*, 2013, **6**, 3249–3253.
- 19 S. Aharon, B. E. Cohen and L. Etgar, Hybrid Lead Halide Iodide and Lead Halide Bromide in Efficient Hole Conductor Free Perovskite Solar Cell, *J. Phys. Chem. C*, 2014, **118**, 17160–17165.
- 20 B. E. Cohen, S. Gamliel and L. Etgar, Parameters Influencing the Deposition of Methylammonium Lead Halide Iodide in Hole Conductor Free Perovskite-Based Solar Cells, *APL Mater.*, 2014, **2**, 081502.
- 21 J. Shi, J. Dong, S. Lv, Y. Xu, L. Zhu, J. Xiao, X. Xu, H. Wu, D. Li and Q. Meng, Hole-Conductor-Free Perovskite Organic Lead Iodide Heterojunction Thin-Film Solar Cells: High Efficiency and Junction Property, *Appl. Phys. Lett.*, 2014, **104**, 063901.
- 22 D. Nanova, A. K. Kast, M. Pfannmoller, C. Muller, L. Veith, I. Wacker, M. Agari, W. Hermes, P. Erk, W. Kowalsky, R. R. Schroder and R. Lovrincic, Unraveling the Nanoscale Morphologies of Mesoporous Perovskite Solar Cells and Their Correlation to Device Performance, *Nano Lett.*, 2014, **14**(5), 2735–2740, DOI: 10.1021/nl5006838.
- 23 T. C. Sum and N. Mathews, Advancements in Perovskite Solar Cells: Photophysics Behind the Photovoltaics, *Energy Environ. Sci.*, 2014, **7**, 2518–2534.
- 24 F. Deschler, M. Price, S. Pathak, L. E. Klintberg, D. D. Jarausch, R. Higgler, S. Hüttner, T. Leijtens, S. D. Stranks, H. J. Snaith, M. Atature, R. T. Phillips and R. H. Friend, High Photoluminescence Efficiency and Optically Pumped Lasing in Solution-Processed Mixed Halide Perovskite Semiconductors, *J. Phys. Chem. Lett.*, 2014, **5**, 1421–1426.
- 25 T. Leijtens, S. D. Stranks, G. E. Eperon, R. Lindblad, E. M. J. Johansson, I. J. McPherson, H. Rensmo, J. M. Ball, M. M. Lee and H. J. Snaith, Electronic Properties of Meso-Superstructured and Planar Organometal Halide Perovskite Films: Charge Trapping, Photodoping, and Carrier Mobility, *ACS Nano*, 2014, **8**(7), 7147–7155, DOI: 10.1021/nn502115k.
- 26 Y. Zhao and K. Zhu, Charge Transport and Recombination in Perovskite (CH_3NH_3) PbI_3 Sensitized TiO_2 Solar Cells, *J. Phys. Chem. Lett.*, 2013, **4**, 2880–2884.
- 27 W. Shockley and H. J. Queisser, Detailed Balance Limit of Efficiency of p–n Junction Solar Cells, *J. Appl. Phys.*, 1961, **32**(3), 510–519.
- 28 I. Borriello, G. Cantele and D. Ninno, Ab initio Investigation of Hybrid Organic-Inorganic Perovskites Based on Tin Halides, *Phys. Rev. B: Condens. Matter Mater. Phys.*, 2008, **77**, 235214.
- 29 G. E. Epron, S. D. Stranks, C. Manelaou, M. B. Johnston, L. M. Herz and H. J. Snaith, Formamidinium lead Trihalide: a Broadly Tunable Perovskite for Efficient Planar Heterojunction Solar Cells, *Energy Environ. Sci.*, 2014, **7**, 982–988.
- 30 S. Lv, S. Pang, Y. Zhou, N. P. Padture, H. Hu, L. Wang, X. Zhou, H. Zhu, L. Zhang and G. Cui, One-step, Solution-processed Formamidinium Lead Trihalide ($\text{FAPbI}_{3-x}\text{Cl}_x$) for Mesoscopic Perovskite-polymer Solar Cells, *Phys. Chem. Chem. Phys.*, 2014, **16**, 19206–19211.
- 31 N. Pellet, P. Gao, G. Gregori, T. Y. Yang, M. K. Nazeeruddin, J. Maier and M. Graetzel, Mixed-Organic-Cation Perovskite Photovoltaics for Enhanced Solar-Light Harvesting, *Angew. Chem., Int. Ed.*, 2014, **53**, 3151–3157.
- 32 S. Pang, H. Hu, J. Zhang, S. Lv, Y. Yu, F. Wei, T. Qin, H. Xu, Z. Liu and G. Cui, $\text{NH}_2\text{CH}=\text{NH}_2\text{PbI}_3$: An Alternative Organolead Iodide Perovskite Sensitizer for Mesoscopic Solar Cells, *Chem. Mater.*, 2014, **26**, 1485–1491.
- 33 A. Dualeh, N. Tétreault, T. Moehl, P. Gao, M. K. Nazeeruddin and M. Grätzel, Effect of Annealing Temperature on Film Morphology of Organic-Inorganic Hybrid Perovskite Solid State Solar Cells, *Adv. Funct. Mater.*, 2014, **24**, 3250–3258.
- 34 T. Supasai, N. Rujisamphan, K. Ullrich, A. Chemseddine and Th. Dittrich, Formation of a passivating $\text{CH}_3\text{NH}_3\text{PbI}_3/\text{PbI}_2$ interface during moderate heating of $\text{CH}_3\text{NH}_3\text{PbI}_3$ layers, *Appl. Phys. Lett.*, 2013, **103**, 183906.
- 35 L. Barnea-Nehoshtan, S. Kirmayer, E. Edri, G. Hodes and D. Cahen, Surface Photovoltage Spectroscopy Study of Organo-Lead Perovskite Solar Cells, *J. Phys. Chem. Lett.*, 2014, **5**, 2408–2413.

- 36 L. Kronik and Y. Shapira, Surface Photovoltage Spectroscopy of Semiconductor Structures: At the Crossroads of Physics, Chemistry and Electrical Engineering, *Surf. Interface Anal.*, 2001, **31**, 954–965.
- 37 E. Mosconi, A. Amat, M. K. Nazeeruddin, M. Grätzel and F. D. Angelis, First-Principles Modeling Of Mixed Halide Organometal Perovskites For Photovoltaic Applications, *J. Phys. Chem. C*, 2013, **117**, 13902–13913.
- 38 A. Usami, S. Seki, Y. Mita, H. Kobayashi, H. Miyashiro and N. Terada, Temperature Dependence of Open-Circuit Voltage in Dye-Sensitized Solar cells, *Sol. Energy Mater. Sol. Cells*, 2009, **93**, 840–842.
- 39 W. L. Leong, G. C. Welch, J. Seifert, J. H. Seo, G. C. Bazan and A. J. Heeger, Understanding the Role of Processing in High Performance Solution Processed Small Molecule Bulk Heterojunction Solar Cells, *Adv. Energy Mater.*, 2013, **3**, 356–363.
- 40 A. J. Frank, N. Kopidakis and J. van de Lagemaat, Electrons in Nanostructured TiO₂ Solar Cells: Transport, Recombination and Photovoltaic Properties, *Coord. Chem. Rev.*, 2004, **248**, 1165–1179.
- 41 Y. Zhao, A. M. Nardes and K. Zhu, Solid-State Mesostuctured Perovskite CH₃NH₃PbI₃ Solar Cells: Charge Transport, Recombination, and Diffusion Length, *J. Phys. Chem. Lett.*, 2014, **5**, 490–494.
- 42 Y. Zhao and K. Zhu, Charge Transport and Recombination in Perovskite (CH₃NH₃)PbI₃ Sensitized TiO₂ Solar Cells, *J. Phys. Chem. Lett.*, 2013, **4**, 2880–2884.
- 43 L. M. Peter and K. G. U. Wijayantha, Electron transport and back reaction in dye sensitized nanocrystalline photovoltaic cells, *Electrochim. Acta*, 2000, **45**, 4543–4551.
- 44 K. Zhu, S.-R. Jang and A. J. Frank, Impact of High Charge-Collection Efficiencies and Dark Energy-Loss Processes on Transport, Recombination, and Photovoltaic Properties of Dye-Sensitized Solar Cells, *J. Phys. Chem. Lett.*, 2011, **2**, 1070–1076.